Hindawi Publishing Corporation
International Journal of Photoenergy
Volume 2016, Article ID 1413072, 8 pages
http://dx.doi.org/10.1155/2016/1413072

Research Article

Influence Applied Potential on the Formation of Self-Organized ZnO Nanorod Film and Its Photoelectrochemical Response

Nur Azimah Abd Samad, Chin Wei Lai, and Sharifah Bee Abd Hamid

Nanotechnology & Catalysis Research Centre (NANOCAT), Institute of Postgraduate Studies (IPS), University of Malaya, 3rd Floor, Block A, 50603 Kuala Lumpur, Malaysia

Correspondence should be addressed to Chin Wei Lai; cwlai@um.edu.my

Received 11 March 2016; Revised 17 April 2016; Accepted 27 April 2016

Academic Editor: Ahmad Umar

Copyright © 2016 Nur Azimah Abd Samad et al. This is an open access article distributed under the Creative Commons Attribution License, which permits unrestricted use, distribution, and reproduction in any medium, provided the original work is properly cited.

The present paper reports on the facile formation of ZnO nanorod photocatalyst electrodeposited on Zn foil in the production of hydrogen gas via water photoelectrolysis. Based on the results, ZnO nanorod films were successfully grown via electrochemical deposition in an optimum electrolyte set of 0.5 mM zinc chloride and 0.1 M potassium chloride at pH level of 5-6 and electrochemical deposition temperature of around 70°C. The study was also conducted at a very low stirring rate with different applied potentials. Applied potential was one of the crucial aspects in the formation of self-organized ZnO nanorod film via control of the field-assisted dissolution and field-assisted deposition rates during the electrochemical deposition process. Interestingly, low applied potentials of 1 V during electrochemical deposition produced a high aspect ratio and density of self-organized ZnO nanorod distribution on the Zn substrate with an average diameter and length of ~37.9 nm and ~249.5 nm, respectively. Therefore, it exhibited a high photocurrent density that reached 17.8 mA/cm^2 under ultraviolet illumination and 12.94 mA/cm^2 under visible illumination. This behaviour was attributed to the faster transport of photogenerated electron/hole pairs in the nanorod's one-dimensional wall surface, which prevented backward reactions and further reduced the number of recombination centres.

1. Introduction

Based on records dating back to 1880 by NASA, Earth's surface temperature was the warmest in 2015 [1]. The outgoing heat absorbed by greenhouse gases, like carbon dioxide, methane, and nitrous oxide, was reemitted in all directions, resulting in the increase of Earth's surface temperature [2]. The emission of greenhouse gases was mostly caused by the combustion of fossil fuels. Therefore, many parties have tried to create alternative energy substitutes to the current energy sources around the world. One of the alternatives is hydrogen gas. In the 21st century, the transition of fuel from liquid to gas phase, commonly known as the hydrogen economy, for future sustainability of fuel and hydrogen-based economies will have an impact on all sectors in the long term.

In this research, ZnO was chosen as the photocatalyst for water splitting applications in hydrogen gas production due to its essential cost-benefit to the industry. ZnO nanorods have high transparency in the visible range and high light trapping characteristics which is very important for PEC water splitting applications [3]. Additionally, the radiation hardness can be applied at high altitudes or even in space with its transparent and conductive properties [4–7]. ZnO has a large number of nanostructures in one-dimensional (1D) form: combs [8], wires [9–11], belts [12, 13], tubes [14–16], spring and ring [17], ribbon, helixes, needle [18], and nanorod [19–21]; two-dimensional (2D) form: nanopellets and nanosheets [22, 23]; and three-dimensional (3D) form: dendrites, flower, dandelion, coniferous structure, and snowflakes [11, 24–29]. In this research, we focused on the formation of ZnO nanorods and studied their morphology, phase, and photochemical responses.

Another convincing motivation arose from the benefits of a one-dimensional (1D) ZnO nanostructure. Since the mobility of electrons was crucial for the formation of hydrogen gas, a 1D nanostructure was selected for this research due to its anisotropic mobility of electrons. The electron mobility increased with the decrease of density for electrons available to scatter. This electron mobility behaviour was attributed to the faster transport of photogenerated electron/hole pairs

Table 1: The revolution of ZnO nanorod formation.

Researchers	Synthesis method	Research findings	References
Azam and Babkair	Low temperature wet chemical method	ZnO nanorod with diameter ~80–90 nm and length ~350–400 nm.	[33]
Abbasi et al.	Hydrothermal growth method	ZnO nanorod with diameter ~150 nm and length ~4 μm on silicon substrate.	[34]
Alvi et al.	Low temperature aqueous chemical growth (ACG) method	Nanowalls, nanorod and nanotubes (diameter ~160 nm, length ~1.2 μm), and nanoflowers. Different precursor and supporting electrolyte produced different nanorod. Pretreated p-GaN substrate.	[35]
Chen et al.	Metalorganic chemical vapor deposition (MOCVD)	ZnO nanorod with diameter ~100 nm on sapphire substrate.	[36]
Badre et al.	Electrochemical deposition method	ZnO nanorod with diameter ~180 nm and length ~1.2 μm on F-doped SnO_2-coated glass substrate.	[37]

in the nanorod's one-dimensional wall surface, which prevented backward reactions and further reduced the number of recombination centres. Many methods were studied by past researchers to form ZnO nanorods (Table 1). However, electrochemical deposition promised the best advantages with benefits like being significantly cost-effective, environmentally friendly, easy to implement, uniform in deposition of materials, reliable, and controllable and having low-energy consumption [30–32].

2. Materials and Methods

2.1. Synthesis of ZnO Nanorod. For the preparation of ZnO nanorods, zinc (Zn) foil (thickness 0.25 mm, 99.9% trace metals basis, Sigma-Aldrich) was dipped in an electrolyte bath composed of 50 mL of 0.5 mM zinc chloride ($ZnCl_2$) and 50 mL of 0.1 M potassium chloride (KCl) at 1.0–3.0 V and under a temperature of 70°C. From our literature studies, a voltage of 1.0 V and temperature of 70°C were selected because the polycrystalline structure of ZnO would start to evolve at this potential difference and temperature with obvious and randomly oriented grains. The as-prepared electrolyte pH was about 5-6 and was measured with a Mettler Toledo InLab Expert Pro pH meter. The electrochemical deposition process was conducted with a two-electrode configuration system, as shown in Figure 1. The platinumelectrode served as the anode while Zn foil served as the cathode. This closed system was then connected to a DC power supply. After the electrochemical deposition, the nanodeposits were then thoroughly rinsed with EMSURE ACS, ISO, Reag. Ph Eur Acetone for analysis and dried at atmosphere. The deposited ZnO nanostructured films were then annealed at 350°C for 3 hours.

2.2. Characterizations of ZnO Nanorod. The photoluminescence spectra, crystallinity, and phase transition of the samples were analysed with a Renishaw In Via Raman microscope and the result was supported with the result of X-ray dispersive (XRD) Bruker D8 Advance that was equipped with EVA Diffract software (Germany) with Cu K radiation

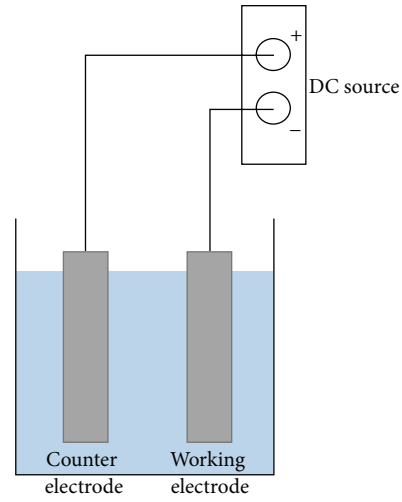

Figure 1: Schematic diagram of electrochemical deposition process.

and wavelength of $\lambda = 1.5418$ Å. Meanwhile, the surface and cross-sectional morphologies of the samples were viewed through JEOL JSM-7600F Field Emission Scanning Electron Microscopy (FESEM) and the elemental analysis of the ZnO nanorod films was determined with a Hitachi Energy Dispersive X-ray (EDX) spectroscopy analysis. To study the photocurrent density of the samples, a three-electrode PEC cell with ZnO nanorod films as the anode, a platinum rod as the cathode, and a saturated calomel electrode (SCE) as the reference electrode was used in a quartz cell filled with 1 M sodium hydroxide (NaOH) containing 1 v% of ethylene glycol. A Newport model 74010 light source was focused on the immersed portion of the photoelectrode to stimulate ultraviolet and visible illumination. All of the three electrodes were connected to the potentiostat (Metrohm Autolab PGSTAT204) and the corresponding current-applied potential value was measured. The photocurrent density was measured with Metrohm Autolab PGSTAT204 with a procedure linear sweep voltammetry potentiostatic applied potential of –1 to 1 V.

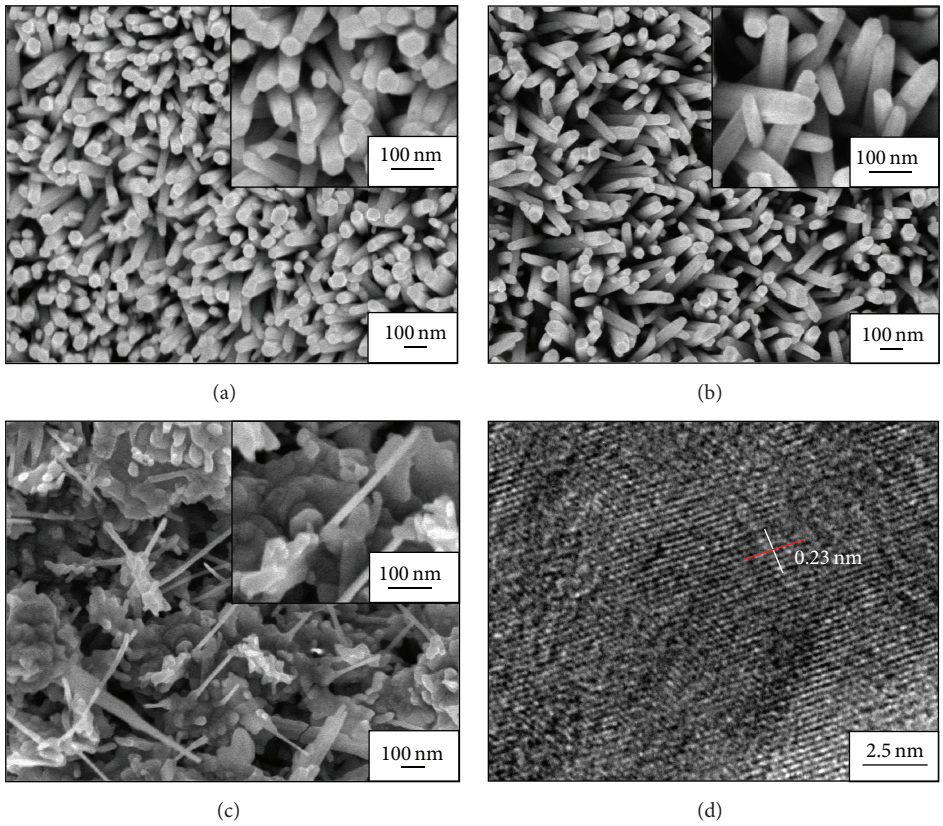

Figure 2: FESEM images: (a) 1 V of electrochemical deposition applied potential; (b) 2 V of electrochemical deposition applied potential; (c) 3 V of electrochemical deposition applied potential. HRTEM image: (d) 1 V of electrochemical deposition applied potential.

3. Results and Discussion

3.1. Morphological Structure of ZnO Nanorod. The appearance of deposited zinc oxide on Zn foil can be said to be dependent on the applied potential during electrodeposition with an optimum set of other variables like 0.5 mM zinc chloride and 0.1 M potassium chloride electrolyte, pH level of ~5-6, electrochemical deposition temperature ~70°C, and a very low stirring rate. Dimensions and uniformity of the morphology of ZnO were a function of the applied potential in the $ZnCl_2$ and KCl electrolyte. For samples deposited under 1 V (Figure 2(a)), nanorods with an average diameter of 37.9 nm and average length of 249.5 nm were produced with near-perfect *c*-direction. When the applied potential was increased to 2 V, the diameter of the nanorods became slightly larger with an average of 61.6 nm but with shorter average lengths of 211.2 nm (Figure 2(b)). In this manner, increases in applied potential produced reductions in lengths as higher precursor dissolution occurred at higher potentials and the Zn^{2+} concentrations were higher in the [0001] direction. Hence, the unit growing in the [1000] direction was preferred and therefore increased in diameter [25, 38]. However, upon achieving steady state, the propagation or crystal growth at direction [1000] would be terminated and the nucleation of new crystals started in the direction of [0001] again. The process would repeat until the applied potential stopped. However, any further increases in applied potential to 3 V would cause irregular features on the surface of the Zn foil and create a dense ZnO structure instead of ordered nanopores that were previously observed. It can be concluded that higher applied potentials produced negative effects on the self-ordering of the deposited zinc oxide, whereby the nanorod structure disappeared and the deposited zinc oxide would be composed of irregular and dense structures with thicknesses of ~2.78 μm, as shown in Figure 2(c). Therefore, a minimum potential of 1 V was found to be optimum for the formation of self-organized ZnO nanorods with lengths approaching 249.5 nm in 60 minutes. On the other hand, the lattice fringes of 1 V samples measured 0.23 nm and indicated (101) ZnO wurtzite (Figure 2(d)).

The final morphology of ZnO nanorods was the competition of field-assisted dissolution and field-assisted deposition of ZnO. By applying higher potentials, strong electric fields helped to accelerate the three-step formation of ZnO nanorods. The driving force of externally applied potential led to the dissolution of $ZnCl_2$, KCl, and water (field-assisted dissolution). Equation (1) shows the dissolution of $KCl + ZnCl_2 + H_2O$. Equation (2) shows the formation of zinc hydroxide ($Zn(OH)_2$). Equation (3) shows the reaction $Zn(OH)_2 + HCl + KOH \rightarrow ZnO + H_2O + KCl$. When the ionic species arrived at the cathode under the influence of applied potential, there was a difference between the actual concentration and solubility concentration (supersaturation) due to the increased local pH of KOH at the cathode which

Table 2: Average compositional ratios for 1 V, 2 V, and 3 V applied potential from EDX spectroscopy.

Element	Atomic percentage (%)		
	1 V	2 V	3 V
Zn	50.3	51.7	55.9
O	49.7	48.3	44.1

produced very high supersaturation. Therefore, in (3), the nucleation of ZnO was started (field-assisted deposition) by the dehydration process of $Zn(OH)_2$ to ZnO [4, 25]. EDX spectroscopy showed averages of 50.3 at% Zn and 49.7 at% O, 51.7 at% Zn and 48.3 at% O, and 55.9 at% Zn and 44.1 at% O for the respective 1 V, 2 V, and 3 V applied potential samples (Table 2). Below are the equations for the formation of ZnO nanorods and a summary of the diameter, length, and aspect ratios of 1 V, 2 V, and 3 V as shown in Table 3.

Dissolution of $KCl + ZnCl_2 + H_2O$ occurs as follows:

$$\begin{aligned} KCl &\longrightarrow K^+(aq) + Cl^-(aq) \\ ZnCl_2 &\longrightarrow Zn^{2+}(aq) + 2Cl^-(aq) \\ 2H_2O &\longrightarrow H_2 \uparrow + 2OH^-(aq) \end{aligned} \quad (1)$$

Formation of zinc hydroxide ($Zn(OH)_2$), KOH, and KCl occurs as follows:

$$\begin{aligned} K^+(aq) + OH^-(aq) &\longrightarrow KOH \\ &\text{(increase in local pH at the cathode)} \\ Zn^{2+}(aq) + 2OH^-(aq) &\longrightarrow Zn(OH)_2 \\ H_2 \uparrow + 2Cl^- &\longrightarrow 2HCl \end{aligned} \quad (2)$$

Formation of zinc oxide (ZnO) occurs as follows:

$$\begin{aligned} Zn(OH)_2 &\longrightarrow ZnO + H_2O \\ &\text{(dehydration process)} \\ HCl + KOH &\longrightarrow H_2O + KCl \end{aligned} \quad (3)$$

3.2. Structural Analysis for ZnO Nanorod. In this study, Raman analysis was used to determine and understand the structural changes of ZnO with different applied potential. Raman inelastic scattering is shown at peak E_2 (high) mode at 438 cm^{-1} and indicated that the ZnO nanostructures' thin film had crystal wurtzite structures with the highest intensity at 1 V (796.5 counts) (Figure 3(a)) as compared to 2 V (468.4 counts) and 3 V (459.7 counts) (Figures 3(b) and 3(c)). However, these thin films in both samples were still weak in pure stoichiometric ZnO due to the dominance of E_1 (LO) and A_1 (LO) mode (570–585 cm^{-1}) as compared to E_2 (high) mode at 438 cm^{-1} and this situation normally occurs in Zn rich ZnO thin films. This can also be due to deficiency in oxygen atoms represented by these two

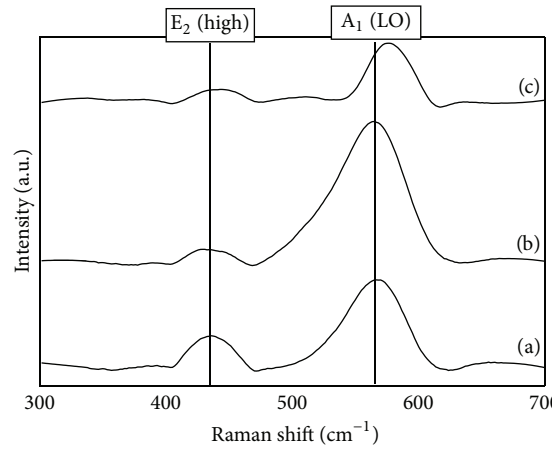

Figure 3: Raman spectra for (a) 1 V, (b) 2 V, and (c) 3 V (excitation: $\lambda = 514$ nm).

modes (E_1 (LO) and A_1 (LO) mode (570–585 cm^{-1})) with the existence of Zn elements from the Zn substrate [39, 40]. Besides this, the shift in the peaks occurred due to the differences in structure. For the 1 V and 2 V sample, it has appeared in the ZnO nanorods and the asymmetric LO phonon peaks were observed at 571 cm^{-1}. Meanwhile, the 3 V samples had dense structures (ZnO bulk crystal); therefore, the frequency of the LO phonon was located at 574 cm^{-1} [41]. In addition to this, many researchers found that the shift occurred at at least 3 cm^{-1} [42–44]. The shift of the peak occurred due to the defects or impurities in the nanocrystals, optical phonon confinement, laser irradiation heating, and the tensile strain effect [41, 45]. Furthermore, the intensity of the peaks was reduced by increasing the applied potential. This occurred due to the quality of the materials which in turn also affected the Raman intensity where higher crystalline quality exhibited higher intensity. Increases in grain size also produced a substantial reduction in asymmetry and intensity of the peaks [46].

The XRD pattern supported the Raman scattering as it showed that the ZnO nanorods were in wurtzite phase which belonged to reference code ICDD 00-036-1451 with a hexagonal crystal system. The plane attributes for this ZnO were 31.7° (100), 34.4° (002), 36.3° (101), 47.5° (102), 56.6° (110), 62.9° (103), and 67.9° (112) (Figure 4). The wurtzite ZnO crystallographic lattice parameters were $a = 3.25$ Å, $b = 3.25$ Å, and $c = 5.21$ Å, which confirmed that the number of alternating planes consisted of O^{2-} and Zn^{2+} that were stacked in tetrahedral structures along the c-axis [47]. 43.2° (101) and 76.9° (004) showed the apparent existence of Zn elements which also reinforced the Raman scattering results (Figure 4).

3.3. Photoluminescence Behaviour. The photoluminescence study for ZnO nanorods was mainly related to some defects, for instance, the zinc vacancies, zinc interstitial, oxygen vacancies, oxygen interstitial, and oxygen antisites. The 350–450 nm region determined the exciton recombination process and is triggered by the recombination of free excitons,

Table 3: Average values for length, diameter, and aspect ratio for different applied potentials.

Potential (V)	Surface morphology	Length (Å)	Diameter (Å)	Average aspect ratio
1	Nanorod	2495 ± 103	379 ± 12	6.58
2	Nanorod	2112 ± 98	616 ± 16	3.43
3	Dense structure	27890 ± 225	—	—

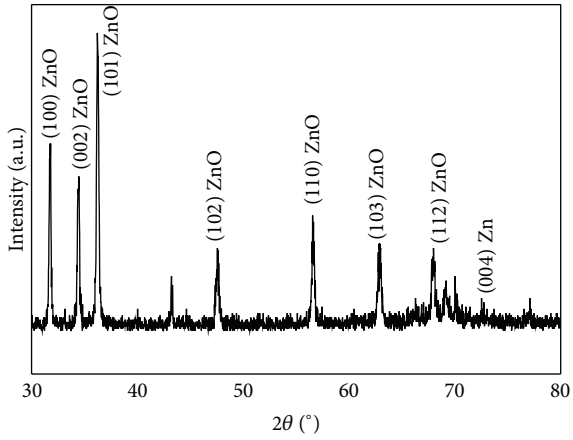

Figure 4: The XRD pattern for ZnO nanorod for 1 V applied potential.

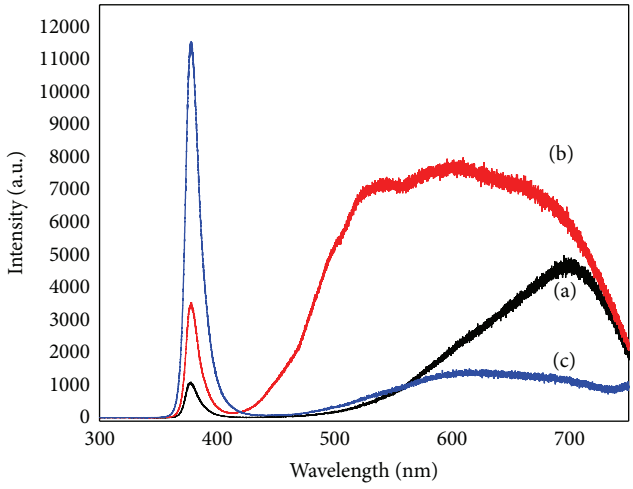

Figure 5: PL spectra for sample: (a) 1 V, (b) 2 V, and (c) 3 V (excitation: λ = 514 nm).

which points to the good crystallinity of the ZnO nanorods [48, 49]. 1 V sample showed the greatest ZnO nanorod crystallinity arrangement since it had the least emissions at the 50–450 nm region (UV region) but small emissions at the 600–700 nm region (orange-red region) indicated small intrinsic defects which was attributed to the presence of small excess oxygen such as oxygen interstitial [50]. This result is supported by EDX which shows a high atomic percentage of oxygen at 49.7% (Figure 5(a)). On the other hand, the sample 2 V showed combinations of more than one defect. Based on the available literature, this could be a combination of an oxygen vacancy and zinc interstitial, V_oZn_i [51]. The origin of green emissions normally came from oxygen based defects [51–54] and a combination of both defects, oxygen vacancy and zinc interstitial defect, produced broad green, yellow, and orange region (Figure 5(b)) [51, 55]. EDX proved that % imbalance occurred in the 2 V sample; the atomic percentage of oxygen (48.3 at%) was lower than that of zinc (51.7 at%). Nevertheless, a few researchers proposed that high volumes of $Zn(OH)_2$ could also produce the broad green, yellow, and orange region [50, 56]. In this case, insufficient annealing was one of the reasons. A second reason would be the rate of field-assisted deposition that was higher compared to the rate of dehydration (formation of ZnO). It therefore produced a high volume of $Zn(OH)_2$ on the nanorod surface. This proposed reason would need further investigation for confirmation. The 3 V sample showed that the superlative performance at the 500–800 nm region for ZnO indicated fewer defects but had very high free exciton recombination at the 350–450 nm region which showed poor crystallinity arrangements of ZnO. The 3 V sample's results indicated that the dense structure was based on its morphology and was in the bulk ZnO as per the results of Raman analysis.

3.4. Photoelectrochemical Response. ZnO with its excellent electronic properties and interfacial stability exhibited great photoelectrochemical response for hydrogen generation. The electrical simulation for water electrolysis (hydrogen generation) was studied by using photoelectrochemical response focusing on the photocurrent density analysis (Figures 6 and 7). Water splitting in excess of 90% occurred with applied potentials of −1 to 1 V [57]. This small current was needed to maintain the double-layer (surface charging and redox reaction) electron flow at the electrodes' surface [58]. A lot of literature has reported that the high active surface areas of photocatalysts generally exhibited excellent photocatalytic and photoelectrochemical responses due to the high percentage of produced and exposed atoms and ions on the catalyst surface. Therefore, a high volume of active sites was crucial for catalytic reactions [59]. Furthermore, the increments in rod lengths provided the fastest way for the charges to be transported along the longitudinal direction of a 1D single-crystalline nanomaterial [58, 59]. In addition, it helped ionic species to have higher driving force in order to move through the barrier layer of the ZnO nanorod tip. The large active area referred to a high average aspect ratio (Table 3).

The 1 V applied potential exhibited the highest photocurrent density, J_p, for ultraviolet illumination (17.8 mA/cm^2) (Figure 6(a)) and visible illumination (12.94 mA/cm^2) (Figure 7(a)) as compared to 2 V (ultraviolet illumination J_p = 11.78 mA/cm^2; visible illumination, J_p = 10.78 mA/cm^2)

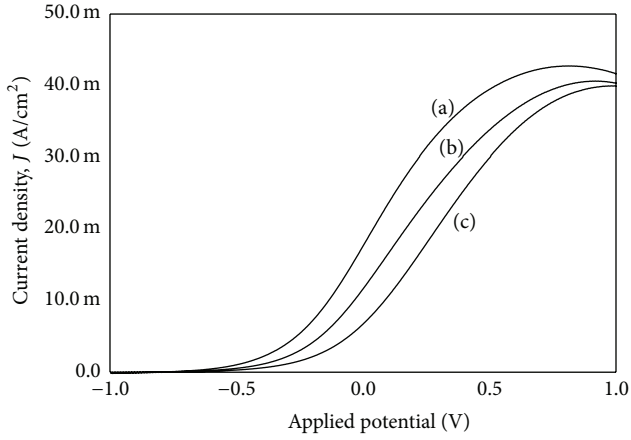

Figure 6: Current density-applied potential characteristics for (a) 1 V, (b) 2 V, and (c) 3 V under ultraviolet illumination.

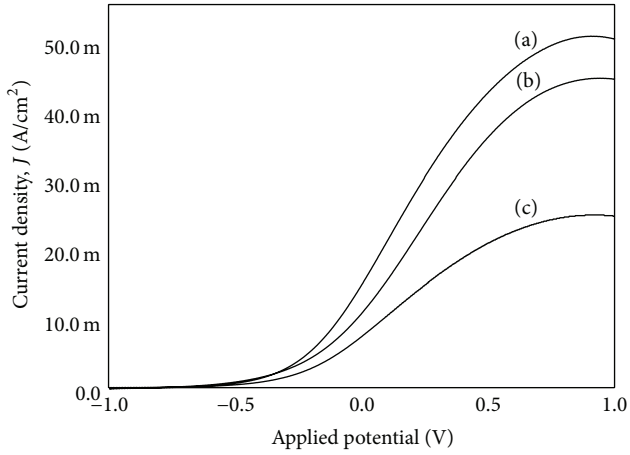

Figure 7: Current density-applied potential characteristics for (a) 1 V, (b) 2 V, and (c) 3 V under visible illumination.

(Figures 6(b) and 7(b)). Based on the above statements, the 1 V applied potential exhibited the highest photocurrent density results due to it possessing the highest aspect ratio as compared to 2 V (Table 3). Meanwhile, the 3 V applied potential exhibited an ultraviolet illumination photocurrent density, J_p, of 6.83 mA/cm^2 and 5.74 mA/cm^2 for visible illumination (Figures 6(c) and 7(c)). The dense porous structures (3 V applied potential) inhibited the charge transfer competence via ZnO (anode) and this charge transfer competence significantly decreased the collection of current density, J, and thus reduced the photocurrent density, J_p, which represented the photoresponse activity.

4. Conclusion

In this paper, it was found that the optimum electrolyte mixture consisted of 0.5 mM zinc chloride and 0.1 M potassium chloride, with pH value of ~5-6, electrochemical deposition temperature of ~70°C, and a very low stirring rate. When this optimum electrolyte mixture was run through an applied potential of 1 V and other important conditions, ZnO nanorods were produced with the highest average aspect ratio morphology. These nanorods also had the highest photocurrent density, J_p, with a value of 17.8 mA/cm^2 under ultraviolet illumination and 12.94 mA/cm^2 under visible illumination. Apart from the phase analysis, the sample ZnO confirmed it was a wurtzite type of ZnO with a number of alternating planes consisting of O^{2-} and Zn^{2+} and had stacked tetrahedral structures along the *c*-axis. The free exciton recombination for 1 V was the lowest as compared to 2 V and 3 V (photoluminescence spectra). However, the small emission region at 600–700 nm (orange-red region) was identified under PL testing. This indicated small intrinsic defects, which was attributed to the presence of small excess of oxygen such as oxygen interstitial.

Competing Interests

The authors declare that there are no competing interests regarding the publication of this paper.

Acknowledgments

The authors would like to thank the University of Malaya for funding this research work under Postgraduate Research Fund Scheme (PPP, PG058-2014B), Fundamental Research Grant Scheme (FP008-2015A), Grand Challenge Grant (GC002A-15SBS), COMSTECH-TWAS Joint Research Grants Programme for Young Scientists (14-316 RG/MSN/AS_C), and Nippon Sheet Glass Foundation for Materials Science and Engineering (IF001-2015).

References

[1] NASA, *NASA, NOAA Analyses Reveal Record-Shattering Global Warm Temperatures in 2015*, 2016, http://www.nasa.gov/press-release/nasa-noaa-analyses-reveal-record-shattering-global-warm-temperatures-in-2015.

[2] NASA, Global Climate Change: Vital Signs of the Planet, 2014, http://climate.nasa.gov/.

[3] S. Ameen, M. S. Akhtar, H.-K. Seo, Y. S. Kim, and H. S. Shin, "Influence of Sn doping on ZnO nanostructures from nanoparticles to spindle shape and their photoelectrochemical properties for dye sensitized solar cells," *Chemical Engineering Journal*, vol. 187, pp. 351–356, 2012.

[4] M. Abd-Ellah, N. Moghimi, L. Zhang et al., "Effect of electrolyte conductivity on controlled electrochemical synthesis of zinc oxide nanotubes and nanorods," *The Journal of Physical Chemistry C*, vol. 117, no. 13, pp. 6794–6799, 2013.

[5] S. Ma, R. Li, C. Lv, W. Xu, and X. Gou, "Facile synthesis of ZnO nanorod arrays and hierarchical nanostructures for photocatalysis and gas sensor applications," *Journal of Hazardous Materials*, vol. 192, no. 2, pp. 730–740, 2011.

[6] Z. Zheng, Z. S. Lim, Y. Peng, L. You, L. Chen, and J. Wang, "General route to ZnO nanorod arrays on conducting substrates via galvanic-cell-based approach," *Scientific Reports*, vol. 3, article 2434, 2013.

[7] A. Janotti and C. G. Van de Walle, "Fundamentals of zinc oxide as a semiconductor," *Reports on Progress in Physics*, vol. 72, no. 12, Article ID 126501, 2009.

[8] T. Xu, P. Ji, M. He, and J. Li, "Growth and structure of pure ZnO micro/nanocombs," *Journal of Nanomaterials*, vol. 2012, Article ID 797935, 5 pages, 2012.

[9] B. Nikoobakht, X. Wang, A. Herzing, and J. Shi, "Scalable synthesis and device integration of self-registered one-dimensional zinc oxide nanostructures and related materials," *Chemical Society Reviews*, vol. 42, no. 1, pp. 342–365, 2013.

[10] L. C. Tien, S. J. Pearton, D. P. Norton, and F. Ren, "Synthesis and microstructure of vertically aligned ZnO nanowires grown by high-pressure-assisted pulsed-laser deposition," *Journal of Materials Science*, vol. 43, no. 21, pp. 6925–6932, 2008.

[11] A. Kołodziejczak-Radzimska and T. Jesionowski, "Zinc oxide—from synthesis to application: a review," *Materials*, vol. 7, no. 4, pp. 2833–2881, 2014.

[12] Z. W. Pan, Z. R. Dai, and Z. L. Wang, "Nanobelts of semiconducting oxides," *Science*, vol. 291, no. 5510, pp. 1947–1949, 2001.

[13] Y. Huang, J. He, Y. Zhang et al., "Morphology, structures and properties of ZnO nanobelts fabricated by Zn-powder evaporation without catalyst at lower temperature," *Journal of Materials Science*, vol. 41, no. 10, pp. 3057–3062, 2006.

[14] J.-J. Wu, S.-C. Liu, C.-T. Wu, K.-H. Chen, and L.-C. Chen, "Heterostructures of ZnO-Zn coaxial nanocables and ZnO nanotubes," *Applied Physics Letters*, vol. 81, no. 7, pp. 1312–1314, 2002.

[15] W. J. Chen, W. L. Liu, S. H. Hsieh, and T. K. Tsai, "Preparation of nanosized ZnO using α brass," *Applied Surface Science*, vol. 253, no. 16, pp. 6749–6753, 2007.

[16] J. Liu, X. Huang, J. Duan, H. Ai, and P. Tu, "A low-temperature synthesis of multiwhisker-based zinc oxide micron crystals," *Materials Letters*, vol. 59, no. 28, pp. 3710–3714, 2005.

[17] X. Y. Kong, Y. Ding, R. Yang, and Z. L. Wang, "Single-crystal nanorings formed by epitaxial self-coiling of polar nanobelts," *Science*, vol. 303, no. 5662, pp. 1348–1351, 2004.

[18] R. Wahab, S. G. Ansari, Y.-S. Kim, H.-K. Seo, and H.-S. Shin, "Room temperature synthesis of needle-shaped ZnO nanorods via sonochemical method," *Applied Surface Science*, vol. 253, no. 18, pp. 7622–7626, 2007.

[19] D. Banerjee, J. Y. Lao, D. Z. Wang et al., "Large-quantity free-standing ZnO nanowires," *Applied Physics Letters*, vol. 83, no. 10, pp. 2061–2063, 2003.

[20] Y.-B. Hahn, "Zinc oxide nanostructures and their applications," *Korean Journal of Chemical Engineering*, vol. 28, no. 9, pp. 1797–1813, 2011.

[21] T. Frade, M. E. Melo Jorge, and A. Gomes, "One-dimensional ZnO nanostructured films: effect of oxide nanoparticles," *Materials Letters*, vol. 82, pp. 13–15, 2012.

[22] W. S. Chiu, P. S. Khiew, M. Cloke et al., "Photocatalytic study of two-dimensional ZnO nanopellets in the decomposition of methylene blue," *Chemical Engineering Journal*, vol. 158, no. 2, pp. 345–352, 2010.

[23] M. José-Yacamán, C. Gutierrez-Wing, M. Miki, D.-Q. Yang, K. N. Piyakis, and E. Sacher, "Surface diffusion and coalescence of mobile metal nanoparticles," *Journal of Physical Chemistry B*, vol. 109, no. 19, pp. 9703–9711, 2005.

[24] V. Polshettiwar, B. Baruwati, and R. S. Varma, "Self-assembly of metal oxides into three-dimensional nanostructures: synthesis and application in catalysis," *ACS Nano*, vol. 3, no. 3, pp. 728–736, 2009.

[25] N. A. Abd Samad, C. W. Lai, and S. B. Abd Hamid, "Easy formation of nanodisk-dendritic ZnO film via controlled electrodeposition process," *Journal of Nanomaterials*, vol. 2015, Article ID 563728, 7 pages, 2015.

[26] Q. Xie, Z. Dai, J. Liang, L. Xu, W. Yu, and Y. Qian, "Synthesis of ZnO three-dimensional architectures and their optical properties," *Solid State Communications*, vol. 136, no. 5, pp. 304–307, 2005.

[27] J. Liu, X. Huang, Y. Li, K. M. Sulieman, F. Sun, and X. He, "Selective growth and properties of zinc oxide nanostructures," *Scripta Materialia*, vol. 55, no. 9, pp. 795–798, 2006.

[28] M. Bitenc and Z. C. Orel, "Synthesis and characterization of crystalline hexagonal bipods of zinc oxide," *Materials Research Bulletin*, vol. 44, no. 2, pp. 381–387, 2009.

[29] G. Lu, X. Wang, J. Liu et al., "One-pot synthesis and gas sensing properties of ZnO mesoporous architectures," *Sensors and Actuators B: Chemical*, vol. 184, pp. 85–92, 2013.

[30] W. Schwarzacher, "Electrodeposition: a technology for the future," *Electrochemical Society Interface*, vol. 15, no. 1, pp. 32–33, 2006.

[31] G. Zangari, "Electrodeposition for energy conversion: electrochemistry over matter," *Electrochemical Society Interface*, vol. 20, no. 2, pp. 31–32, 2011.

[32] I. M. Dharmadasa and J. Haigh, "Strengths and advantages of electrodeposition as a semiconductor growth technique for applications in macroelectronic devices," *Journal of the Electrochemical Society*, vol. 153, no. 1, pp. G47–G52, 2006.

[33] A. Azam and S. S. Babkair, "Low-temperature growth of well-aligned zinc oxide nanorod arrays on silicon substrate and their photocatalytic application," *International Journal of Nanomedicine*, vol. 9, no. 1, pp. 2109–2115, 2014.

[34] M. A. Abbasi, Y. Khan, S. Hussain, O. Nur, and M. Willander, "Anions effect on the low temperature growth of ZnO nanostructures," *Vacuum*, vol. 86, no. 12, pp. 1998–2001, 2012.

[35] N. H. Alvi, S. M. Usman Ali, S. Hussain, O. Nur, and M. Willander, "Fabrication and comparative optical characterization of n-ZnO nanostructures (nanowalls, nanorods, nanoflowers and nanotubes)/p-GaN white-light-emitting diodes," *Scripta Materialia*, vol. 64, no. 8, pp. 697–700, 2011.

[36] H.-G. Chen, S.-R. Jian, Z.-W. Li, K.-W. Chen, and J.-C. Li, "Epitaxial growth of self-arranged periodic ZnO nanostructures on sapphire substrates grown by MOCVD," *Journal of Alloys and Compounds*, vol. 504, no. 1, pp. S368–S371, 2010.

[37] C. Badre, P. Dubot, D. Lincot, T. Pauporte, and M. Turmine, "Effects of nanorod structure and conformation of fatty acid self-assembled layers on superhydrophobicity of zinc oxide surface," *Journal of Colloid and Interface Science*, vol. 316, no. 2, pp. 233–237, 2007.

[38] X. Y. Zhang, J. Y. Dai, C. H. Lam et al., "Zinc/ZnO core-shell hexagonal nanodisk dendrites and their photoluminescence," *Acta Materialia*, vol. 55, no. 15, pp. 5039–5044, 2007.

[39] G. J. Exarhos and S. K. Sharma, "Influence of processing variables on the structure and properties of ZnO films," *Thin Solid Films*, vol. 270, no. 1-2, pp. 27–32, 1995.

[40] M. Schumm, M. Koerdel, J. F. Morhange et al., "Analysis of the vibrational properties of $Zn_{1-x}Co_xO$ by Raman spectroscopy," *Journal of Physics: Conference Series*, vol. 92, no. 1, Article ID 012149, 2007.

[41] K. Dai, T. Peng, H. Chen, R. Zhang, and Y. Zhang, "Photocatalytic degradation and mineralization of commercial methamidophos in aqueous Titania suspension," *Environmental Science and Technology*, vol. 42, no. 5, pp. 1505–1510, 2008.

[42] H.-M. Cheng, H.-C. Hsu, Y.-K. Tseng, L.-J. Lin, and W.-F. Hsieh, "Raman scattering and efficient UV photoluminescence from well-aligned ZnO nanowires epitaxially grown on GaN buffer layer," *The Journal of Physical Chemistry B*, vol. 109, no. 18, pp. 8749–8754, 2005.

[43] Z. Wang, H. Zhang, L. Zhang, J. Yuan, S. Yan, and C. Wang, "Low-temperature synthesis of ZnO nanoparticles by solid-state pyrolytic reaction," *Nanotechnology*, vol. 14, no. 1, pp. 11–15, 2003.

[44] Y. Yang, H. Yan, Z. Fu, B. Yang, and J. Zuo, "Correlation between 577 cm^{-1} Raman scattering and green emission in ZnO ordered nanostructures," *Applied Physics Letters*, vol. 88, no. 19, Article ID 191909, 2006.

[45] K. A. Alim, V. A. Fonoberov, and A. A. Balandin, "Origin of the optical phonon frequency shifts in ZnO quantum dots," *Applied Physics Letters*, vol. 86, no. 5, Article ID 053103, 3 pages, 2005.

[46] C. Roy, S. Byrne, E. McGlynn et al., "Correlation of Raman and X-ray diffraction measurements of annealed pulsed laser deposited ZnO thin films," *Thin Solid Films*, vol. 436, no. 2, pp. 273–276, 2003.

[47] Z. L. Wang, "Zinc oxide nanostructures: growth, properties and applications," *Journal of Physics: Condensed Matter*, vol. 16, no. 25, pp. R829–R858, 2004.

[48] C. Chandrinou, N. Boukos, C. Stogios, and A. Travlos, "PL study of oxygen defect formation in ZnO nanorods," *Microelectronics Journal*, vol. 40, no. 2, pp. 296–298, 2009.

[49] X.-Y. Shen, Y.-C. Zhai, and Y.-H. Zhang, "Preparation and characterization of ultrafine zinc oxide powder by hydrothermal method," *Transactions of Nonferrous Metals Society of China*, vol. 20, no. 1, pp. s236–s239, 2010.

[50] A. B. Djurišić, Y. H. Leung, K. H. Tam et al., "Defect emissions in ZnO nanostructures," *Nanotechnology*, vol. 18, no. 9, Article ID 095702, 2007.

[51] N. H. Alvi, *Luminescence Properties of ZnO Nanostructures and Their Implementation as White Light Emitting Diodes (LEDs)*, Linköping University, 2011.

[52] F. A. Kröger and H. J. Vink, "The origin of the fluorescence in self-activated ZnS, CdS, and ZnO," *The Journal of Chemical Physics*, vol. 22, no. 2, pp. 250–252, 1954.

[53] S. A. Studenikin, N. Golego, and M. Cocivera, "Fabrication of green and orange photoluminescent, undoped ZnO films using spray pyrolysis," *Journal of Applied Physics*, vol. 84, no. 4, pp. 2287–2294, 1998.

[54] S. Yamauchi, Y. Goto, and T. Hariu, "Photoluminescence studies of undoped and nitrogen-doped ZnO layers grown by plasma-assisted epitaxy," *Journal of Crystal Growth*, vol. 260, no. 1-2, pp. 1–6, 2004.

[55] A. Janotti and C. G. Van de Walle, "Native point defects in ZnO," *Physical Review B*, vol. 76, no. 16, Article ID 165202, 2007.

[56] H. Zhou, H. Alves, D. M. Hofmann et al., "Behind the weak excitonic emission of ZnO quantum dots: ZnO/$Zn(OH)_2$ core-shell structure," *Applied Physics Letters*, vol. 80, no. 2, pp. 210–212, 2002.

[57] S. Licht, B. Wang, S. Mukerji, T. Soga, M. Umeno, and H. Tributsch, "Over 18% solar energy conversion to generation of hydrogen fuel; theory and experiment for efficient solar water splitting," *International Journal of Hydrogen Energy*, vol. 26, no. 7, pp. 653–659, 2001.

[58] G. A. Crawford and N. Chawla, "Porous hierarchical TiO_2 nanostructures: processing and microstructure relationships," *Acta Materialia*, vol. 57, no. 3, pp. 854–867, 2009.

[59] C. W. Lai and S. Sreekantan, "Effect of applied potential on the formation of self-organized TiO_2 nanotube arrays and its photoelectrochemical response," *Journal of Nanomaterials*, vol. 2011, Article ID 142463, 7 pages, 2011.

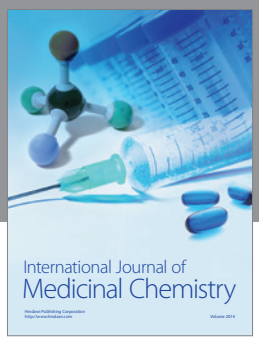

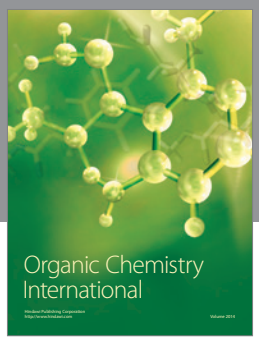

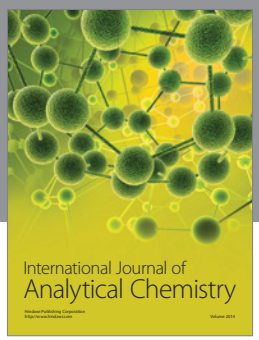

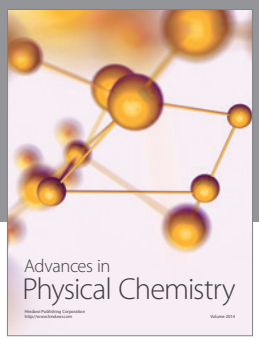

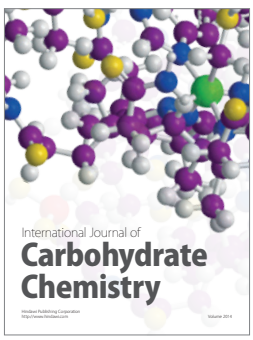

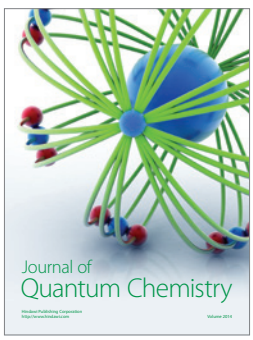

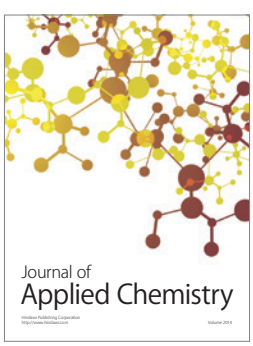

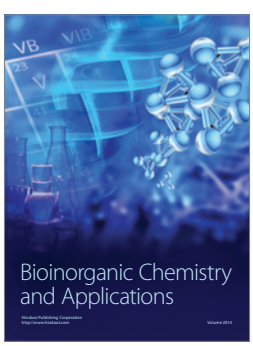

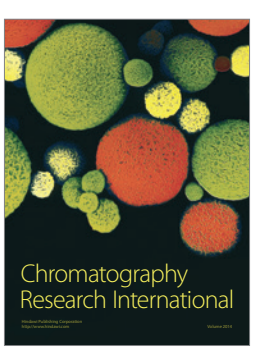

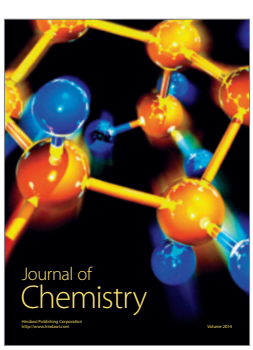

Hindawi

Submit your manuscripts at
http://www.hindawi.com